


Hyperbolic Polaritons in Topological Nodal Ring Semimetals

Ashutosh Singh,^{1,2,*} Maria Sebastian¹, Yuanping Chen,³ Po-Yao Chang^{2,†} and Alexey Belyanin^{1,‡}

¹Department of Physics and Astronomy, Texas A&M University, College Station, Texas 77843, USA

²Department of Physics, National Tsing Hua University, Hsinchu 300013, Taiwan

³School of Physics and Electronic Engineering, Jiangsu University, Zhenjiang, 212013, Jiangsu, China

 (Received 31 March 2023; revised 14 June 2023; accepted 9 August 2023; published 1 September 2023)

In mirror-symmetric systems, there is a possibility of the realization of extended gapless electronic states characterized as nodal lines or rings. Strain induced modifications to these states lead to the emergence of different classes of nodal rings with qualitatively different physical properties. Here we study optical response and the electromagnetic wave propagation in type I nodal ring semimetals, in which the low-energy quasiparticle dispersion is parabolic in momentum k_x and k_y and is linear in k_z . This leads to a highly anisotropic dielectric permittivity tensor in which the optical response is plasmonic in one spatial direction and dielectric in the other two directions. The resulting normal modes (polaritons) in the bulk material become hyperbolic over a broad frequency range, which is furthermore tunable by the doping level. The propagation, reflection, and polarization properties of the hyperbolic polaritons not only provide valuable information about the electronic structure of these fascinating materials in the most interesting region near the nodal rings but also pave the way to tunable hyperbolic materials with applications ranging from anomalous refraction and waveguiding to perfect absorption in ultrathin subwavelength films.

DOI: [10.1103/PhysRevLett.131.096902](https://doi.org/10.1103/PhysRevLett.131.096902)

Introduction.—The quantification of topological properties of condensed matter systems in the last decade has been driven to a large extent by the studies of Dirac and Weyl semimetals [1,2]. In these materials, the conduction and the valence bands merge at isolated points in the Brillouin zone such that the low-energy quasiparticles mimic the physics of Dirac and Weyl fermions with speed much lower than light. Low-energy optical spectroscopy provides a unique opportunity for their energy-resolved studies near band crossings, which is not always possible by other means. Perhaps the most direct consequence of the Weyl fermion dispersion is a linear in frequency conductivity [3–7], with modifications due to the anisotropic dispersion [8] band with temperature playing an important role due to the quadratic dependence of density of states on quasiparticle energy [9,10]. A lot of effort has been spent on extracting the topological features of these materials from their optical properties; see, e.g., [11–15] and references therein.

In a rather new class of topological semimetals known as nodal line semimetals, the conduction and valence band touch along a line or a ring (loop) [16]. Different classes of nodal rings have been proposed, e.g., hybrid nodal rings [17], spin gapless nodal rings [18], topological nodal rings in carbon networks [19], antiperovskites [20], semimetallic carbon tetrarings [21], and orthorhombic C_{16} [22]. Table I in [23] contains a useful list of predicted or identified nodal line semimetals. Among many interesting features displayed by the nodal ring semimetals (NRSMs) are unusual Landau level quantization [24], and drumhead surface states [25,26]. Furthermore, the bulk energy

dispersion is highly anisotropic in momentum space as shown in Figs. 1(a) and 1(b). Moreover, an abrupt change in Fermi surface topology occurs when the quasiparticle energy is tuned in the vicinity of the energy gap parameter [Fig. 1(c)]. A direct consequence of this feature appears in the density of states (DOS), Fig. 1(d).

One can fully expect that these unusual electronic properties of NRSMs result in a peculiar and even unique optical response. Previous studies were mainly focused on the derivation and characterization of the linear optical conductivity spectra [27–29] including the effect of tilt [30,31] as well as the second-order conductivity in symmetry-broken NRSMs [32]. However, the aspect of the optical response which provides most insight into the physical properties, and also the one most closely connected to experiment, is the behavior of the normal electromagnetic (EM) modes of the material, or the polaritons. In this Letter we focus on the most prevalent type I NRSMs in which the connection between the fascinating properties of the polaritons and the underlying electronic structure is very intuitive. The salient property of the polaritons in NRSMs stems from the fact that the low-energy quasiparticle dispersion is parabolic in momentum k_x and k_y but is linear in k_z . This leads to uniaxial anisotropy of the dielectric permittivity tensor in which the optical response is plasmonic in one spatial direction and dielectric in the other two directions. The resulting polaritons in the bulk material split into so-called ordinary and extraordinary modes, and the extraordinary mode becomes hyperbolic over a broad frequency range, which is furthermore tunable by the doping level.

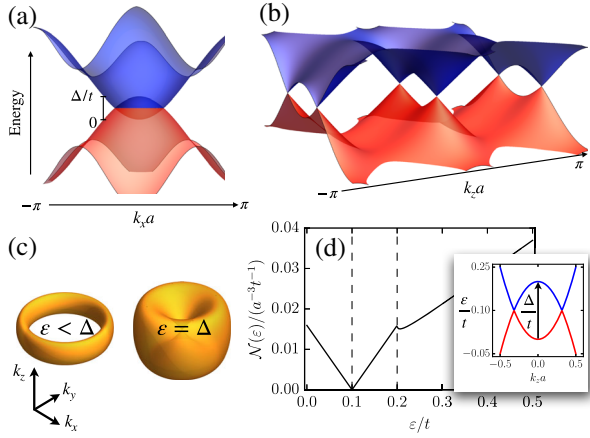


FIG. 1. Energy dispersion in (a) $k_z = 0$, and (b) $k_y = 0$ momentum planes for type-I NRSMs described by the Hamiltonian in Eq. (1). The vertical axis is normalized by t . (c) Constant energy surfaces. For energies lower than Δ the momentum distribution forms a toroidal shape. Increasing energy deforms the toroid and it collapses into a drumlike structure for energies greater than Δ . (d) The density of states, $\mathcal{N}(\epsilon)$, normalized by $a^{-3}t^{-1}$ as a function of energy ϵ normalized by t for $\Delta = 0.2t$.

Note that in “conventional” nodal-point Weyl semimetals the hyperbolic dispersion was only predicted in high magnetic fields and with Fermi level tuned to the band crossing points [11]. In the prototypical nodal line semimetal ZrSiSe the hyperbolic dispersion has been recently observed with tip-enhanced infrared spectroscopy [33]. In other kinds of anisotropic crystals, such as hexagonal boron nitride, the hyperbolic dispersion typically exists only in a narrow midinfrared frequency range defined by the separation between anisotropic phonon resonances [34]. Yet another group of hyperbolic materials that received a lot of recent interest is metamaterials where hyperbolicity is achieved at certain wavelengths and propagation angles by periodic combination of metallic and dielectric layers [35,36]. These hyperbolic materials are highly sought after for numerous applications as they exhibit a plethora of unique properties such as negative refraction, propagation through subwavelength apertures, and waveguiding by ultrathin films.

Thus, our study connects two rapidly growing areas of physics research, namely, topological materials and hyperbolic optical materials, and therefore represents a useful bridge between the condensed matter community and hyperbolic optics community. Starting from the effective but quite general Hamiltonian for topological nodal rings, we derive explicit analytic expressions connecting topological electron eigenstates and the properties of propagating EM eigenmodes for the whole class of these fascinating materials. Our results reveal that nodal ring semimetals represent a nontrivial and perhaps even unique route to hyperbolicity through the highly unusual electron properties of the bulk crystal which hosts both relativistic (massless) as

well as nonrelativistic fermions, contributing to the optical response within the same frequency range.

Electron states in NRSMs.—Our effective Hamiltonian, which describes different types of NRSMs, is based on the low-energy Hamiltonian from [19], but we included a finite band curvature which makes all integrals over the Brillouin zone finite while keeping the same low-energy electronic structure in the vicinity of the nodal rings:

$$H(\mathbf{k}) = \begin{pmatrix} t_1 \mathcal{G}(k_x, k_y) & it_2 \sin(k_z a) \\ -it_2 \sin(k_z a) & \Delta + \gamma t_1 \mathcal{G}(k_x, k_y) \end{pmatrix}, \quad (1)$$

where $\mathcal{G}(k_x, k_y) = 2 - \cos(k_x a) - \cos(k_y a)$, t_1 and t_2 are the hopping parameters, a is the lattice spacing, Δ is the gap at the Γ point and γ is the band tuning parameter which takes the value -1 for type-I NRSMs and $0 < \gamma < 1$ for type-II NRSMs. A third class of topological NRSMs comprises of merging type-I and type-II materials for which γ as well as $\mathcal{G}(k_x, k_y)$ changes. The nodal lines are protected by the mirror symmetry M_z , $M_z^{-1}H(\mathbf{k})M_z = H(\bar{\mathbf{k}})$ with $\bar{\mathbf{k}} = (k_x, k_y, -k_z)$ and $M_z = \sigma_z$. One can visualize the nodal lines as the Berry flux tubes in the momentum space. These Berry flux tubes are robust objects due to quantization of the flux to integer multiples of π .

In this Letter, we focus on type-I nodal rings with $\gamma = -1$, and we further take $t_1 = t_2 = t$ to reduce the number of material parameters. Since t_1 and t_2 enter the Hamiltonian (1) as multiplicative factors, all derivation steps can be easily repeated for $t_1 \neq t_2$ if needed for specific compounds, following the detailed derivation in the Supplemental Material (SM) [37]. One should expect the lattice constant a to be of the order of 0.1–0.3 nm, whereas the hopping energy t is typically on the scale of several eV. To fix the numerical value of the product at for the plots, we assume that the “Fermi velocity” v_F , i.e., the linear slope of the electron dispersion in Fig. 1(b), satisfies $\hbar a^{-1}v_F = t$, whereas its ratio to the speed of light is $v_F/c = 1/300$. This is true by an order of magnitude for most Dirac materials. The parameter Δ could vary in wide limits. The most optimal situation for optical studies of topological nodal ring states is when Δ is small as compared to t , so that the nodal rings and characteristic optical transitions at photon energies $\sim \Delta$ are near the center of the Brillouin zone and well separated from higher-energy transitions between any trivial remote bands. As we see below, this will also maximize the optical anisotropy. We will set $\Delta = 0.2t$ for further discussion. The corresponding electron energy dispersion is shown in Fig. 1.

The quasiparticle energy dispersion for the Hamiltonian in Eq. (1) is given as

$$\epsilon_{\lambda\mathbf{k}} = \frac{\Delta}{2} + \frac{\lambda}{2} \sqrt{[\Delta - 2\mathcal{G}(k_x, k_y)t]^2 + 4t^2 \sin^2(k_z a)}, \quad (2)$$

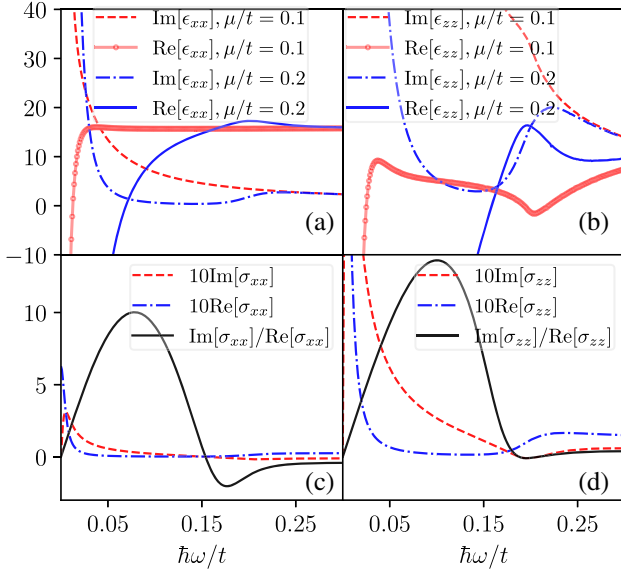


FIG. 2. Top row: real and imaginary parts of (a) ϵ_{xx} and (b) ϵ_{zz} as a function of photon energy, for two different values of the chemical potential. The value of $\mu/t = 0.1$ corresponds to the chemical potential exactly at the band crossing, as one can see from Fig. 1(d). Bottom row: the spectra of (c) xx and (d) zz components of the conductivity tensor normalized by $(e^2/\hbar a)$. Solid curves: the ratio of imaginary to real part of the conductivity components.

where $\lambda = +1(-1)$ for the conduction (valence) band. In the electric dipole approximation the interband optical transitions are vertical. The transition energy for a quasiparticle at momentum \mathbf{k} is given by the difference between the conduction and the valence band energies,

$$\hbar\omega_{\mathbf{k}} = \sqrt{[\Delta - 2\mathcal{G}(k_x, k_y)]^2 + 4t^2 \sin^2(k_z a)}. \quad (3)$$

The normalized eigenvectors are

$$|\Psi_{\lambda\mathbf{k}}\rangle = \frac{1}{\mathcal{N}_\lambda} \begin{pmatrix} i(-\Delta + 2t\mathcal{G}(k_x, k_y) + \lambda\hbar\omega_{\mathbf{k}}) \\ 2t \sin(k_z a) \end{pmatrix}, \quad (4)$$

with $\mathcal{N}_\lambda = \sqrt{[-\Delta + 2t\mathcal{G}(k_x, k_y) + \lambda\hbar\omega_{\mathbf{k}}]^2 + 4t^2 \sin^2(k_z a)}$.

Optical permittivity.—In equilibrium at temperature T and chemical potential μ , the linear response optical conductivity is computed within the Kubo framework [38]. We will take $k_B T = t/200$ for numerical plots to include thermally excited carriers. In order to incorporate scattering-related losses at the phenomenological level, we have introduced a decay rate, $\hbar\Gamma = 0.005t$. For the hopping energy $t \sim 3$ eV this corresponds to significant disorder, with scattering time ~ 40 fs. The current operator components are $\hat{j}_\alpha = e\hbar^{-1}\partial_{k_\alpha}\hat{H}$, where $\alpha = \{x, y, z\}$. For the Hamiltonian (1) they become

$$\hat{\mathbf{j}} = \frac{eat}{\hbar} \{\sin(k_x a)\hat{\sigma}_z, \sin(k_y a)\hat{\sigma}_z, -\cos(k_z a)\hat{\sigma}_y\}. \quad (5)$$

We also add the background permittivity (ϵ_b) due to the sum of contributions from remote bands not included in the Hamiltonian (1), and assume it to be isotropic and with negligible dispersion within the frequency range of interest to us. Its exact value shifts the plots in Fig. 2 but does not change the qualitative physical behavior; we will use $\epsilon_b = 15$ as a reasonable number in the infrared. The resulting dielectric tensor $\hat{\epsilon}$ is expressed in terms of the conductivity (in SI units) as $\hat{\epsilon}(\omega) = \epsilon_b \mathbb{I}_{3 \times 3} + i\hat{\sigma}(\omega)/(\omega\epsilon_0)$. Because of the symmetry of the system, only the diagonal terms of the conductivity tensor survive. The details of the conductivity derivation and analytic results are provided in the SM. The general structure and scaling of the diagonal permittivity components are given by $\epsilon_{\alpha\alpha}(\omega) = \epsilon_b - g\alpha_F c \mathcal{I}_{\alpha\alpha}/(2\pi^2 a\omega)$, where $\mathcal{I}_{\alpha\alpha}$ are dimensionless integrals specified in the SM, $\alpha_F = e^2(4\pi\epsilon_0\hbar c)^{-1}$ is the fine structure constant, and c is the speed of light.

To the leading order in the long wavelength limit, cylindrical symmetry is preserved so that $\epsilon_{yy} \approx \epsilon_{xx}$. However, ϵ_{zz} behaves differently, as shown in Fig. 2. First of all, the magnitude of the matrix elements of the j_z component of the current is higher than the ones for $j_{x,y}$ components, as one can see from Eq. (5) and the SM. Indeed, when $\Delta \ll t$ the main contribution comes from the states with $|k_\alpha a| \ll 1$ in the vicinity of the nodal rings. In this case the ratio of matrix elements $|j_z/j_{x,y}| \sim t/\Delta \gg 1$, yielding a higher magnitude of ϵ_{zz} as compared to ϵ_{xx} . Second, while at the lowest frequencies all permittivity components are dominated by an intraband plasmonic response (even when the Fermi level is at the band crossing energy, $\mu/t = 0.1$, because free carriers are still present at finite temperature), with increasing frequency and doping level the behavior of ϵ_{xx} becomes dielectric, whereas the ϵ_{zz} component maintains plasmonic behavior over a significantly broader frequency range. This extreme anisotropy with opposite signs of the real parts of the dielectric tensor components gives rise to the hyperbolic dispersion of the polaritons. The exact bandwidth of the hyperbolic response depends on the material parameters and the doping level. For example, if we take $t \sim 3$ eV and $\mu = 0.2t$, it is equal to ~ 300 meV and the range of hyperbolic dispersion is located between wavelengths of about 2.4 and 6 μm . This range will increase for lower values of the background dielectric permittivity. It will also be affected by the presence of a tilt in the electron dispersion. Indeed, the broad region of hyperbolicity originates from the large ratio of zz vs xx components of the Drude weight. If there is a tilt in electron dispersion along the z axis, this would further increase the respective Drude weight and the region of hyperbolicity would further broaden. Vice versa, a tilt in the x direction is expected to reduce the spectral region where hyperbolicity is observed.

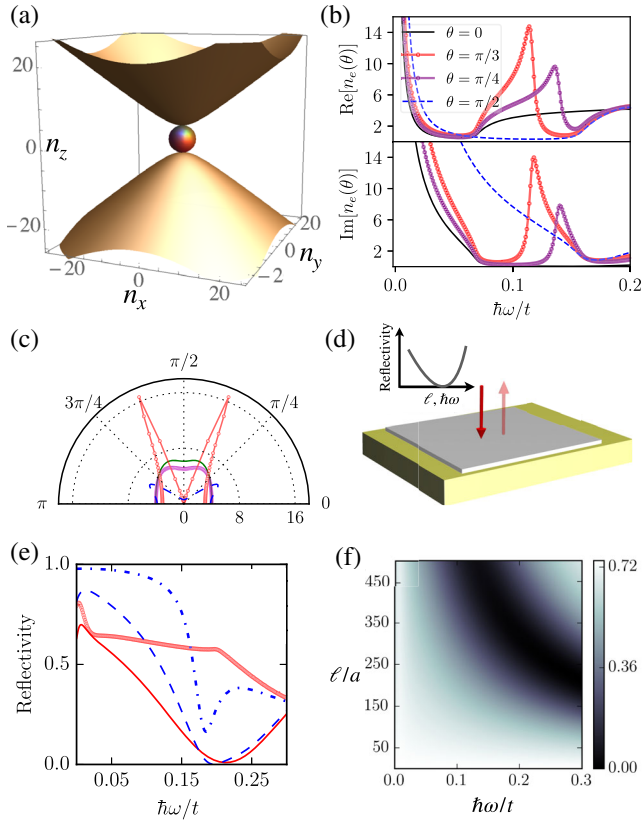


FIG. 3. (a) The solution of the dispersion equation (6) for the extraordinary wave (yellow hyperboloid) and ordinary wave (red sphere) at a constant photon energy $\hbar\omega \sim 0.13t$ and $\mu = 0.2t$, so that $\epsilon_{xx} \sim 13$ and $\epsilon_{zz} \sim -20$. (b) $\text{Re}[n_e]$ and $\text{Im}[n_e]$ as a function of photon energy for $\mu = 0.2t$ and four propagation angles θ . (c) Real part of $n_e(\theta)$ for $\mu = 0.1t$, $\hbar\omega = 0.1t$ (solid green), $\mu = 0.1t$, $\hbar\omega = 0.15t$ (purple triangle), $\mu = 0.2t$, $\hbar\omega = 0.1t$ (red circles), and $\mu = 0.2t$, $\hbar\omega = 0.15t$ (dashed blue). (d) Schematic for the reflection of a normally incident EM wave from an ultrathin NRSM film of thickness ℓ placed on top of a substrate of complex refractive index n_d . (e) Ordinary (extraordinary) wave reflectivity shown in red line (circles) for $\mu = 0.1t$, and in dashed blue line (dot-dashed line) for $\mu = 0.2t$. The film thickness $\ell = 300a$. (f) Color plot of the ordinary wave reflectivity for $\mu = 0.1t$ as a function of the thickness of the film (y axis) and the photon frequency (x axis). Here we assumed $n_d = 1.4 + 4.0i$.

Figures 2(c) and 2(d) show the conductivity spectra. The ratios $\{\text{Im}[\sigma_{xx}]/\text{Re}[\sigma_{xx}]\}$ and $\{\text{Im}[\sigma_{zz}]/\text{Re}[\sigma_{zz}]\}$ demonstrate broad peaks in the spectral region of hyperbolic dispersion, indicating the possibility of low-loss propagation of hyperbolic polaritons; compare with other hyperbolic materials in Fig. 4 of Ref. [33].

Properties of NRSM polaritons.—Maxwell’s equations for the electric field vector $\mathbf{E} \propto \exp(i\mathbf{q}\mathbf{r} - i\omega t)$ of monochromatic EM waves propagating in a bulk crystal with permittivity tensor $\hat{\epsilon}$ can be written as

$$\mathbf{n}(\mathbf{n} \cdot \mathbf{E}) - n^2\mathbf{E} + \hat{\epsilon}\mathbf{E} = 0, \quad (6)$$

where $\mathbf{n} = \mathbf{q}c/\omega$. For a diagonal permittivity tensor, the solution of the corresponding dispersion equation consists of two linearly polarized normal modes (polaritons) which are often called an ordinary and extraordinary wave. Since $\epsilon_{yy} = \epsilon_{xx}$, we can consider without loss of generality the propagation with the wave vector in the (xz) plane, i.e., $\mathbf{n} = (n_x, 0, n_z)$. Then the refractive indices of the ordinary and extraordinary modes are given by

$$n_o^2 = \epsilon_{xx} \quad \text{and} \quad n_e^2 = \frac{\epsilon_{xx}\epsilon_{zz}}{\epsilon_{xx}\sin^2\theta + \epsilon_{zz}\cos^2\theta}, \quad (7)$$

where $\theta = \cos^{-1}(n_z/|\mathbf{n}|)$. The electric field vector of the extraordinary mode lies in the (xz) plane, whereas the one of the ordinary mode is along y .

Figure 3(a) shows an example of the constant-frequency surface for the dispersion equation of the two modes. The surfaces are plotted for $\mu = 0.2t$ and the frequency $\hbar\omega \sim 0.13t$ for which the real parts of the dielectric tensor components have a much greater magnitude than the imaginary parts, so that $\epsilon_{xx} \sim 13$ and $\epsilon_{zz} \sim -20$. For the ordinary waves, the surface is a sphere, which is a particular case of the usual Fresnel ellipsoid. At the same time, for the extraordinary modes, the surface is a hyperboloid. Its cross section at $n_y = 0$ is

$$\frac{n_x^2}{\epsilon_{zz}} + \frac{n_z^2}{\epsilon_{xx}} = 1. \quad (8)$$

In the range of frequencies where $\text{Re}[\epsilon_{zz}] < 0$ and $\text{Re}[\epsilon_{xx}] > 0$ the EM waves are able to propagate in certain directions with $|\mathbf{n}| \gg 1$, i.e., $|\mathbf{q}| \gg \omega/c$, as one can also see in Fig. 3(c). Note that we neglected the imaginary parts of the dielectric tensor only in Fig. 3(a), whereas in Figs. 3(b), 3(c), and 3(e) a full dielectric tensor with its real and imaginary parts is used. That is why the maximum refractive index is finite in Fig. 3(c), although it is quite large, almost 20. Note also that the frequency at which the high- q propagation regime with maximum refractive index is reached depends on the propagation angle θ and shifts to higher frequencies with decreasing θ as indicated in Fig. 3(b).

The dominant feature in the spectra of hyperbolic polaritons is a characteristic peak in the extraordinary wave dispersion and absorption near the frequency which minimizes the denominator in the expression (7) for n_e^2 , see the spectra in Fig. 3(b). The resonance exists for any angle $\theta \neq 0$ or $\pi/2$. A similar phenomenon in classical anisotropic plasmas would be a hybrid plasmon-polariton resonance, corresponding to hybridization between longitudinal plasmons and transverse EM waves. Note also the existence of a photonic band gap at frequencies above the resonance, where the real part of the refractive index would have dropped to zero in the absence of an imaginary part of the permittivity tensor. The real part of the refractive index drops

very steeply at the photonic band gap boundary, indicating a small group velocity $v_{\text{group}} \ll c$ in this region. This behavior is similar to the dispersion of extraordinary magnetopolaritons in nodal-point Weyl semimetals [11].

Obviously, all of the above spectral and angular features in polariton propagation and absorption can have important practical applications in thin-film EM waveguides, modulators, switches etc. We will mention just one more potential application, which has been pointed out for strongly absorbing materials: ultrathin-film perfect absorbers [39]. Consider an EM wave normally incident on an ultrathin (strongly subwavelength) NRSM film, as in Fig. 3(d). In this case destructive interference between reflections from the front and back facets of the film can result in spectral windows of zero reflectivity even for a film much thinner than the incident wavelength. This is illustrated in Fig. 3(e) for a fixed film thickness and in Fig. 3(f) for a range of thicknesses of a few tens of nm, depending on the exact value of the lattice period a . The zero reflectivity region is tunable by doping, film thickness, and also depends on the substrate. As was shown in [39], the best results are obtained for metallic or highly doped semiconducting substrates with mostly an imaginary refractive index, such as the one chosen for Figs. 3(e) and 3(f).

In conclusion, topological nodal ring semimetals are natural hyperbolic optical materials, with associated extreme optical anisotropy, anomalous refraction, and strong plasmon-polariton resonances. Their unique combination of optical properties is highly sensitive to the material parameters and can be used for optical spectroscopy of the nodal rings. Ultrathin films of NRSMs can find a number of applications as infrared waveguides, modulators, switches, and antireflection coatings.

This work has been supported in part by the Air Force Office for Scientific Research Grant No. FA9550-21-1-0272 and National Science Foundation Grant No. 1936276. P. Y. C. is supported by the Young Scholar Fellowship Program by National Science and Technology Council (NSTC) in Taiwan, under Grant No. 112-2636-M-007-007.

*asingh.n19@gmail.com

†prayser@gmail.com

‡belyanin@tamu.edu

- [1] N. P. Armitage, E. J. Mele, and A. Vishwanath, *Rev. Mod. Phys.* **90**, 015001 (2018).
- [2] A. Burkov, *Annu. Rev. Condens. Matter Phys.* **9**, 359 (2018).
- [3] R. Y. Chen, S. J. Zhang, J. A. Schneeloch, C. Zhang, Q. Li, G. D. Gu, and N. L. Wang, *Phys. Rev. B* **92**, 075107 (2015).
- [4] A. B. Sushkov, J. B. Hofmann, G. S. Jenkins, J. Ishikawa, S. Nakatsuji, S. Das Sarma, and H. D. Drew, *Phys. Rev. B* **92**, 241108(R) (2015).
- [5] B. Xu, Y. M. Dai, L. X. Zhao, K. Wang, R. Yang, W. Zhang, J. Y. Liu, H. Xiao, G. F. Chen, A. J. Taylor, D. A. Yarotski, R. P. Prasankumar, and X. G. Qiu, *Phys. Rev. B* **93**, 121110(R) (2016).
- [6] D. Neubauer, J. P. Carbotte, A. A. Nateprov, A. Löhle, M. Dressel, and A. V. Pronin, *Phys. Rev. B* **93**, 121202(R) (2016).
- [7] T. Timusk, J. P. Carbotte, C. C. Homes, D. N. Basov, and S. G. Sharapov, *Phys. Rev. B* **87**, 235121 (2013).
- [8] J. P. Carbotte, *Phys. Rev. B* **94**, 165111 (2016).
- [9] A. Singh and J. P. Carbotte, *Phys. Rev. B* **99**, 235134 (2019).
- [10] A. Singh and J. P. Carbotte, *Phys. Rev. B* **103**, 075114 (2021).
- [11] Z. Long, Y. Wang, M. Erukhimova, M. Tokman, and A. Belyanin, *Phys. Rev. Lett.* **120**, 037403 (2018).
- [12] H. Rostami and M. Polini, *Phys. Rev. B* **97**, 195151 (2018).
- [13] Q. Chen, A. R. Kutayiah, I. Oladyskhin, M. Tokman, and A. Belyanin, *Phys. Rev. B* **99**, 075137 (2019).
- [14] Q. Chen, M. Erukhimova, M. Tokman, and A. Belyanin, *Phys. Rev. B* **100**, 235451 (2019).
- [15] J. E. Moore, *Natl. Sci. Rev.* **6**, 206 (2018).
- [16] C. Fang, H. Weng, X. Dai, and Z. Fang, *Chin. Phys. B* **25**, 117106 (2016).
- [17] Z. J. Chen, Z. J. Xie, Y. J. Jin, G. Liu, and H. Xu, *Phys. Rev. Mater.* **6**, 034202 (2022).
- [18] T. Yang, Z. Cheng, X. Wang, and X.-L. Wang, *J. Adv. Res.* **28**, 43 (2021).
- [19] Y. Gao, Y. Chen, Y. Xie, P.-Y. Chang, M. L. Cohen, and S. Zhang, *Phys. Rev. B* **97**, 121108(R) (2018).
- [20] R. Yu, H. Weng, Z. Fang, X. Dai, and X. Hu, *Phys. Rev. Lett.* **115**, 036807 (2015).
- [21] Y. Cheng, X. Feng, X. Cao, B. Wen, Q. Wang, Y. Kawazoe, and P. Jena, *Small* **13**, 1602894.
- [22] J.-T. Wang, H. Weng, S. Nie, Z. Fang, Y. Kawazoe, and C. Chen, *Phys. Rev. Lett.* **116**, 195501 (2016).
- [23] L. Xu, X. Zhang, W. Meng, T. He, Y. Liu, X. Dai, Y. Zhang, and G. Liu, *J. Mater. Chem. C* **8**, 14109 (2020).
- [24] J.-W. Rhim and Y. B. Kim, *Phys. Rev. B* **92**, 045126 (2015).
- [25] Y.-H. Chan, C.-K. Chiu, M. Y. Chou, and A. P. Schnyder, *Phys. Rev. B* **93**, 205132 (2016).
- [26] G. Bian, T.-R. Chang, H. Zheng, S. Velury, S.-Y. Xu, T. Neupert, C.-K. Chiu, S.-M. Huang, D. S. Sanchez, I. Belopolski, N. Alidoust, P.-J. Chen, G. Chang, A. Bansil, H.-T. Jeng, H. Lin, and M. Z. Hasan, *Phys. Rev. B* **93**, 121113(R) (2016).
- [27] S. P. Mukherjee and J. P. Carbotte, *Phys. Rev. B* **95**, 214203 (2017).
- [28] S. Barati and S. H. Abedinpour, *Phys. Rev. B* **96**, 155150 (2017).
- [29] A. V. Pronin and M. Dressel, *Phys. Status Solidi (b)* **258**, 2000027 (2021).
- [30] S. Ahn, E. J. Mele, and H. Min, *Phys. Rev. Lett.* **119**, 147402 (2017).
- [31] Y. Shao, Z. Sun, Y. Wang, and D. N. Basov, *Proc. Natl. Acad. Sci. U.S.A.* **116**, 1168 (2018).
- [32] J. W. Zuber and C. Zhang, *Phys. Rev. B* **103**, 205307 (2021).

- [33] Y. Shao, A. J. Sternbach, B. S. Y. Kim, A. A. Rikhter, X. Xu, U. D. Giovannini, R. Jing, S. H. Chae, Z. Sun, S. H. Lee, Y. Zhu, Z. Mao, J. C. Hone, R. Queiroz, A. J. Millis, P. J. Schuck, A. Rubio, M. M. Fogler, and D. N. Basov, *Sci. Adv.* **8**, eadd6169 (2022).
- [34] A. J. Sternbach, S. L. Moore, A. Rikhter, S. Zhang, R. Jing, Y. Shao, B. S. Y. Kim, S. Xu, S. Liu, J. H. Edgar, A. Rubio, C. Dean, J. Hone, M. M. Fogler, and D. N. Basov, *Science* **379**, 555 (2023).
- [35] A. Poddubny, I. Iorsh, P. Belov, and Y. Kivshar, *Nat. Photonics* **7**, 948 (2013).
- [36] I. I. Smolyaninov, *Hyperbolic Metamaterials* (Morgan and Claypool Publishers, San Rafael, 2018), pp. 2053–2571.
- [37] See Supplemental Material at <http://link.aps.org/supplemental/10.1103/PhysRevLett.131.096902> for details of the derivation.
- [38] G. D. Mahan, *Many-Particle Physics* (Springer US, New York, 1990).
- [39] J. Rensberg, Y. Zhou, S. Richter, C. Wan, S. Zhang, P. Schöppe, R. Schmidt-Grund, S. Ramanathan, F. Capasso, M. A. Kats, and C. Ronning, *Phys. Rev. Appl.* **8**, 014009 (2017).